Axial-azimuthal high-frequency instability modes in a Hall thruster fluid model

IEPC-2019-687

Presented at the 36th International Electric Propulsion Conference
University of Vienna, Austria
September 15-20, 2019

Enrique Bello-Benítez* and Eduardo Ahedo†
Space Propulsion and Plasma group (EP2), Universidad Carlos III de Madrid, Leganés, Spain

Turbulence, azimuthal oscillations and instabilities in Hall thrusters can effectively contribute to the cross-field electron transport. In this work, stability and high-frequency oscillations in the Hall-thruster discharge are studied in the axial-azimuthal plane with a linear fluid perturbation model, accounting for global effects, such as plasma inhomogeneity and boundary conditions. The proposed perturbation model includes electron pressure effects in the electron momentum equation, that are disregarded in some high-frequency analyses. The effect of electron temperature perturbations on stability is discussed by comparing results with and without first-order temperature terms in the electron momentum equation. These results suggest that electron temperature should not be overlooked in high-frequency stability analyses. For the case with no temperature perturbations, the stability analysis is complemented with a parametric study and a comparison with local dispersion relations. The impact of oscillations on electron transport is assessed, including contributions from inertia, which are usually not taken into account and are noted to be nonnegligible according to our results.

Nomenclature

$\boldsymbol{E}, \boldsymbol{B}$	= electric and magnetic field vectors
E, B	= electric and magnetic field magnitudes
x, y, z	= radial, azimuthal and axial coordinate
t	= time
$\mathbf{1}_x, \mathbf{1}_y, \mathbf{1}_z$	= unitary vector in the radial, azimuthal and axial direction
ω	= complex frequency
ω_r	= oscillation frequency (real part of ω)
γ	= growth rate (imaginary part of ω)
k_y, k_z	= azimuthal and axial wave numbers
λ_y	= azimuthal wavelength
L	= typical length of axial variation of macroscopic variables
n	= plasma density
n_e, n_i	= electron and ion number density
ν_e	= electron collision frequency
ν_i	= ionization frequency
ν_w, ν_{we}	= wall particle-loss and energy-loss frequency
E_i'	= energy loss per particle due to ionization and radiation
$\mathbf{u}_e, \mathbf{u}_i, \mathbf{u}_n$	= electron, ion and neutral fluid velocity vectors

*PhD. Student, Bio-Engineering and Aerospace Engineering Department. ebello@ing.uc3m.es
†Professor, Bio-Engineering and Aerospace Engineering Department. eahedo@ing.uc3m.es

u_{jk}	= fluid velocity in the j-th direction (y, z) of k-th species (e, i)
ϕ, T_e	= electric potential and electron temperature
$\boldsymbol{q}_e$	= electron heat flow vector
q_{ye}, q_{ze}	= electron heat flow vector in the azimuthal and axial direction
e, m_e, m_i	= electron charge, and electron and ion masses
c_s, c_e	= sound and electron thermal speed
φ	= generic macroscopic variable
$\varphi_0, \tilde{\varphi}_1$	= zeroth and first-order macroscopic variable
φ_1	= complex amplitude of first order macroscopic variable
ω_{ce}	= electron cyclotron frequency
ω_{lh}	= lower-hybrid frequency
χ	= Hall parameter
N	= number of points in discretization
$\Gamma_e, \Gamma_i, \Gamma_n, \Gamma_m$	= flux of electrons, ions, neutrals and mass
$\dot{m}_A$	= mass flow rate through the anode
g_m, g_c	= mass flux and total current densities
V_d	= discharge voltage
L_{ch}, d_c, R	= length, width and mean radius of the channel
z_{max}	= location of the maximum magnetic field with respect to the anode
L_{AN}	= distance from anode to external cathode
α_B	= anomalous diffusion coefficient
$\tilde{\nu}_w$	= dimensionless parameter for the wall losses model
T_{SEE}	= electron temperature yielding 100% of secondary electron emission
a_w	= accommodation factor
L_{m1}, L_{m2}	= characteristic lengths of the magnetic field profile in the channel and in the plume
I_d	= discharge current
u_{ph}	= oscillation phase speed
F_{yt}	= equivalent azimuthal force produced by oscillations

I. Introduction

Numerical simulations of Hall thrusters are not currently able to accurately reproduce the large cross-field electron transport observed empirically,[1] especially close to exit of the channel. Classical collisional theories fail in predicting the electron transport, so that there must be collisionless transport mechanisms that are not yet fully understood. In macroscopic electron models, this is typically solved by adding extra collisionality with tunable parameters. However, this approach is not useful to reach predictive models that could be used for design tasks. Plasma turbulence and oscillations in the azimuthal direction have been considered to possibly explain this *anomalous* electron current by correlated azimuthal oscillations of plasma density and azimuthal electric field producing an axial drift.[2] Other contributions from oscillations to transport, than the one we have just mentioned, are considered in this work.

The complex physical phenomena taking place in Hall thrusters lead to a wide variety of azimuthal oscillations at different scales and frequency regimes.[3] At low frequencies (5-25 kHz), rotating spokes have been observed in the near-anode region and unconventionally long channels.[2] Although the physical phenomena leading to the formation of spokes is unclear, some of its characteristic have been successfully reproduced in nonlinear kinetic[4] and fluid[5] simulations; and with linear fluid stability analysis.[6]

The low-to-medium frequency band (20-500 kHz) is occupied by gradient drift instabilities, as

measured in experiments.[7] Dispersion relations with homogeneous background plasma has been proposed that show instability criteria based on magnetic and density gradients,[8] and predict oscillations with significant azimuthal component in the close-anode and near-plume regions.[9]

In the high-frequency range (1-10 MHz) azimuthal instabilities, close to the channel exit and near plume regions, are observed at two different scales:

- Hall thruster circumference. The mean value is close to 27 cm in the SPT-100 model, with average radius $R = 4.25$ cm. Azimuthal waves travelling with phase speed of the order of the electron drift velocity have been observed experimentally and predicted theoretically.[10] This speed has been shown to be fairly constant along the channel, which suggest the presence of non-local mechanisms. This is the reason why there are multiple examples in the literature of high-frequency global stability analysis,[11–13] using a macroscopic formulation for all species in the plasma. Electron inertia has been noted to play an important role, since it is fundamental in the existence and derivation of the corresponding dispersion relation.[10]
- Electron Larmor radius ℓ_e and smaller. This is of the order of millimeters for typical values of Hall thrusters. It was introduced theoretically, using kinetic dispersion relations, in the 1970s[14, 15] as the Electron Cyclotron Drift Instability (ECDI), and it is attracting the interest of the scientific community because of anomalous cross-field electron transport. The theory predicts that this instability can develop in $\mathbf{E} \times \mathbf{B}$ plasmas with homogeneous background. Experiments[16] show two azimuthally counter-propagating waves at scales 1.14-0.70 mm with phase velocity 2.5 km/s (this is of the order of the ion sound speed for electron temperature $T_e \approx 8.6$ eV). From the theory and simulation perspective, the approach used to study this modes is purely kinetic.[17, 18] There is no evidence (to the best of our knowledge) on the capabilities of macroscopic models to capture this instability.

Although at different scales, these two types of azimuthal instabilities have common features: the frequency range and axial location close to the channel exit. The big difference in the orders of magnitude of phase speeds is directly related to the difference in scale. It is not completely cleat if the ECDI could be reproduced by fluid models or whether there is a connection between the two introduced types of electron drift waves.

This work attempts to complete global high-frequency stability analyses in fluid models by extending them to smaller scaler scales. It has been noted that cold electrons are usually assumed in similar analyses (Ref. 13 is a good summary of fluid perturbation models in this frequency regime), which do not seem justified in all regions of the discharge and, thus, is not suitable for studying instabilities with a global approach. Moreover, the fluid equations are simplified in such a way that one single differential equation is reached for the perturbation potential, removing any effect from boundary conditions involving other variables (among other possible effects).

In Sec. II the model used to study the stability of the Hall thruster discharge is introduced. The proposed perturbation model minimizes the number of assumptions, while still keeping those that are reasonable in the high-frequency regime (e.g. neglecting ionization or decoupling of neutral species). In Sec. III results are shown and discussed assuming negligible electron temperature oscillations. This assumption is undone in Sec. IV and the results are compared with previous ones.

II. Perturbation fluid model

The presence of instabilities is studied using a small perturbation method and a fluid description for every species in the plasma: singly-charged Xenon ions, electrons and neutral Xenon (sub-indexes i, e and n, respectively). Under this approach, the plasma variables are expressed as

$$\varphi(y, z, t) = \varphi_0(z) + \tilde{\varphi}_1(y, z, t) \tag{1}$$

where φ represents every plasma variable, z is the coordinate along the thruster axis (with origin at the anode) and y is the azimuthal coordinate pointing in the direction of the electron drift (thus, x is the radial coordinate). This is, the complete solution is separated into a stationary axisymmetric background (φ_0) and a small peturbation ($\tilde{\varphi}_1$), which contains the non-stationary

and azimuthal behavior. The plasma variables used in this work should be understood as radially averaged, which leads to the appearance of source terms in macroscopic equations accounting for plasma-wall interaction effects.[19]

The axial evolution of background, or zeroth-order, variables come as equilibrium solutions to the stationary axisymmetric fluid equations,[19] for given value of parameters. Then, the temporal and spatial evolution of small perturbations (the first order solution) is approximately governed by linearized fluid equations. This linear system is, in addition, homogeneous. In our analysis, perturbation equations are Fourier-transformed in time and azimuthal coordinates, i.e.

$$\tilde{\varphi}_1(y,z,t) = \mathrm{Re}\{\varphi_1(z)\exp\left(-i\omega t + ik_y y\right)\} \tag{2}$$

where φ_1 is the complex amplitude of the waves and keeps the axial dependence of the perturbations. Then, the set of fluid equations form a system of ordinary differential equations that govern the axial behavior of the complex amplitudes of first order variables. Solving this type of problem with the corresponding boundary conditions is a global approach to stability.

The Fourier expansion can be also made in z, under which the derivative operator $\mathrm{d}/\mathrm{d}z$, applied to first order variables in the equations, becomes ik_z. This is strictly valid in the limit of the Boussinesq approximation $k_z L \gg 1$ (which is not satisfied, in general, in Hall thrusters due to important inhomogeneities in the background plasma), where L is a characteristic length associated to the background plasma gradients. This approach is local, in the sense that stability can be studied at each z independently, with frozen values of background variables and gradients. Moreover, local dispersion relations cannot account for the effect of boundary conditions. This work focuses on the global approach, but we try to establish a connection between local and global results.

Regarding boundary conditions (required in the axial direction), both the complete perturbed solution and the background plasma satisfy the same ones. This fact can be used to obtain first order boundary conditions, which are homogeneous.

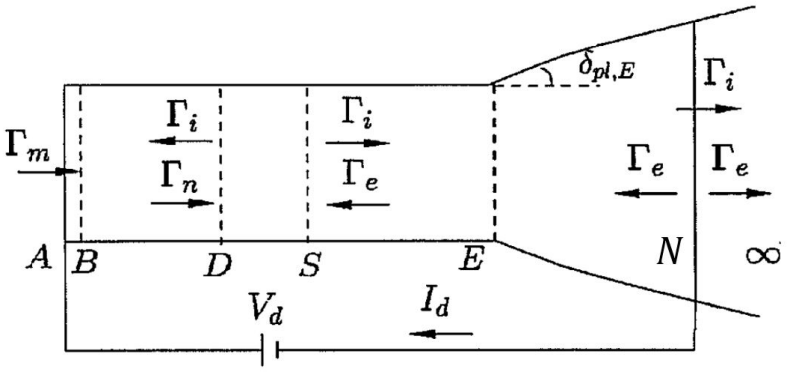

Figure 1: Schematic representation of a Hall thruster,[20] with V_d being the discharge voltage, I_d the discharge current and $\Gamma_{i,e,n,m}$ the ion, electron, neutral and mass fluxes.

An schematic view of a Hall-thruster discharge is displayed in Fig. 1, which shows relevant axial positions. The considered discharge region extends from the anode wall (A) to the cathode or neutralized (N). It contains the thuster channel (from A to E) and a portion of the near plume (from E to N). Points D and S are located at the positions of quiescent and interior sonic ions. Point B denotes the anode sheath edge, where the quasineutral plasma region starts and ions are also sonic but flowing towards the anode wall. Both zeroth and first order solutions are assumed to satisfy quasineutrality from B to N (which will be later checked) and, thus, quasineutral models are used in a domain from B to N. An anode sheath model is used to translate boundary conditions from A to B.

Table 2: Nominal parameters of the SPT-100 Hall thruster, where $\dot{m}_A$ is the mass flow at the anode, V_d is the discharge voltage, B_{max} is the maximum magnitude of the magnetic field (located at z_{max}), L_{ch} is the channel length, L_{AE} is the anode-cathode length, d_c is the channel width, R is the average channel radius, T_{eN} is the temperature of cathode electrons, u_{znB} is the injection velocity of neutrals, $L_{m1,2}$ are characteristic lengths for the magnetic field profile and α_B, $\tilde{\nu}_w$, T_{SEE} and a_w are parameters required for collisional and wall-interaction models.[19]

$\dot{m}_A$	4.75 mg/s	V_d	300 V
B_{max}	251 G	z_{max}	2.5 cm
L_{ch}	2.5 cm	L_{AE}	3.35 cm
d_c	1.5 cm	R	4.25 cm
T_{eN}	5 eV	u_{znB}	300 m/s
α_B	0.094	$\tilde{\nu}_w$	0.17
T_{SEE}	36.8 eV	a_w	0.85
L_{m1}	1.5 cm	L_{m2}	0.5 cm

A. Two-dimensional macroscopic model

Due to the assumptions made on the first order problem (introduced later in this section), the perturbation neutral equations are uncoupled from other species. They are required, though, in order to solve for the background[19] plasma behavior. The macroscopic transport equations, only for ion and electron species, for the sake of conciseness, read

$$\frac{\partial n}{\partial t} + \nabla \cdot (n\boldsymbol{u}_i) = n(\nu_i - \nu_w) \tag{3a}$$

$$\frac{\partial \boldsymbol{u}_i}{\partial t} + \boldsymbol{u}_i \cdot \nabla \boldsymbol{u}_i = -\frac{e}{m_i}\nabla\phi + \nu_i\left(\boldsymbol{u}_n - \boldsymbol{u}_i\right) \tag{3b}$$

$$\frac{\partial n}{\partial t} + \nabla \cdot (n\boldsymbol{u}_e) = n(\nu_i - \nu_w) \tag{3c}$$

$$\frac{\partial \boldsymbol{u}_e}{\partial t} + \boldsymbol{u}_e \cdot \nabla \boldsymbol{u}_e = -\frac{1}{m_e n}\nabla\left(nT_e\right) + \frac{e}{m_e}\left(\nabla\phi - \boldsymbol{u}_e \times \boldsymbol{B}\right) - \nu_e \boldsymbol{u}_e \tag{3d}$$

$$\frac{\partial}{\partial t}\left(\frac{3}{2}nT_e\right) + \nabla \cdot \left(\frac{3}{2}nT_e\boldsymbol{u}_e\right) = nT_e\nabla \cdot \boldsymbol{u}_e - \nabla \cdot \boldsymbol{q}_e - n\nu_i E_i' - n\nu_{we}T_e + m_e n\nu_e u_e^2 \tag{3e}$$

$$0 = \frac{5}{2}nT_e\nabla T_e + e\boldsymbol{q}_e \times \boldsymbol{B} + m_e\nu_e\boldsymbol{q}_e \tag{3f}$$

where n is the quasineutral plasma density, $\boldsymbol{u}_i = u_{zi}\mathbf{1}_z$ is the ion velocity vector, $\boldsymbol{u}_e = u_{ye}\mathbf{1}_y + u_{ze}\mathbf{1}_z$ is the electron velocity vector, ϕ is the electric potential, T_e is the electron temperature, $\boldsymbol{q}_e = q_{ye}\mathbf{1}_y + q_{ze}\mathbf{1}_z$ is the electron heat flow vector, $\boldsymbol{B} = B\mathbf{1}_x$ is the magnetic field vector, ν_i is the ionization frequency, ν_w is the wall particle-loss frequency, ν_e is the total electron collision frequency, ν_{we} is the wall energy-loss frequency, E_i' accounts for energy losses due to ionization and radiation, e is the electron charge in absolute value, m_i is the ion mass and m_e is the electron mass. The macroscopic variables are averaged over the width d_c. The plume expansion produces an increase in d_c, which is neglected for the purposes of this work. The electron inertia has been neglected in

the heat flow transport[a] (Eq. (3f)).

The boundary conditions of background and perturbed plasma variables are:

1. The total discharge current I_d flowing through the electric circuit. It can be shown to be equal to the total current (contribution of ions and electrons) next to the cathode plane. That is to say
$$g_c = en_N \left(u_{ziN} - u_{zeN}\right) \tag{4}$$
where $g_c \equiv I_d/(2\pi R d_c)$.

2. The ion axial velocity u_{zi} satisfies the Bohm condition $u_{ziB} = -c_{sB}$ at the anode sheath edge, with $c_s = \sqrt{T_e/m_i}$ being the ion sonic speed.

3. The anode wall potential is set to zero. In the zeroth order problem, this condition fixes the arbitrary reference potential. The potential at the sheath edge follows[20]
$$\frac{e\phi_B}{T_{eB}} = \ln\sqrt{\frac{T_{eB}}{2\pi m_e u_{zeB}^2}} \tag{5}$$
provided that $\phi_A = 0$. This expression comes from a stationary, unmagnetized, collisionless and isothermal macroscopic sheath model and the required matching with the quasineutral particle flux at the sheath edge.

4. The heat flux at the anode sheath edge (q_{zeB}) can be also estimated as
$$q_{zeB} = n_B u_{zeB}\left(e\phi_{AB} - \frac{1}{2}T_{eB}\right) \tag{6}$$
that ensures matching with the axial heat flow from the sheath model.[21]

5. The temperature of injected electrons at the cathode plane (T_{eN}).

6. The azimuthal velocity of injected electrons (u_{yeN}). Being able to satisfy this condition requires keeping electron inertia terms in the azimuthal equation of motion. Electron diffusive models, such as the one used here to compute the background plasma response, make mathematically impossible to force a boundary condition for u_{ye}.

7. Total mass flow (contribution of neutrals and recombined ions) injected at the anode, which is expressed as
$$g_m = m_i \left(u_{ziB} n + u_{znB}\right) \tag{7}$$
where $g_m \equiv \dot{m}_A//(2\pi R d_c)$.

8. Injection velocity of neutrals at the anode sheath edge (u_{znB}).

9. A boundary condition is required at interior sonic points (where the ion axial velocity satisfies $u_{zi}^2 = T_e/m_i$) that ensures a smooth transition between subsonic and supersonic regions of the discharge.[20] Sonic singularities can only be allowed at sheath edges.

The zeroth order plasma solution is integrated with these boundary conditions[20] and the perturbations must be such that the perturbed plasma solution satisfies them as well. The calculation of the zeroth order solution is not described in this document since it has been thoroughly explored in the literature.[19–21]

B. First order model

For the perturbation model, it is assumed that: (*i*) the perturbed ion motion is purely axial, (*ii*) collision frequencies are not perturbed, (*iii*) properties of neutrals are not perturbed and (*iv*) perturbations are quasi-neutral ($\tilde{n}_1 \equiv \tilde{n}_{e1} = \tilde{n}_{i1}$) and electrostatic. Using the small perturbation

[a]While this is consistent in the zeroth order solution, it is not in first order. A fully consistent perturbation model would require to include inertial terms in the electron heat flow equation.

approach in Eq. (1) and the fact that the background plasma profiles are solution to stationary axisymmetric equations, yield

$$u_{zi0}\frac{\mathrm{d}n_1}{\mathrm{d}z} + n_0\frac{\mathrm{d}u_{zi1}}{\mathrm{d}z} = \left(i\omega - \frac{\mathrm{d}u_{zi0}}{\mathrm{d}z}\right)n_1 - \frac{\mathrm{d}n_0}{\mathrm{d}z}u_{zi1} \equiv F_1 \tag{8a}$$

$$u_{zi0}\frac{\mathrm{d}u_{zi1}}{\mathrm{d}z} + \frac{e}{m_i}\frac{\mathrm{d}\phi_1}{\mathrm{d}z} = \left(i\omega - \frac{\mathrm{d}u_{zi0}}{\mathrm{d}z}\right)u_{zi1} \equiv F_2 \tag{8b}$$

$$u_{ze0}\frac{\mathrm{d}n_1}{\mathrm{d}z} + n_0\frac{\mathrm{d}u_{ze1}}{\mathrm{d}z} = \left(i\omega - ik_y u_{ye0} - \frac{\mathrm{d}u_{ze0}}{\mathrm{d}z}\right)n_1 - \frac{\mathrm{d}n_0}{\mathrm{d}z}u_{ze1} - ik_y n_0 u_{ye1} \equiv F_3 \tag{8c}$$

$$\begin{aligned} u_{ze0}\frac{\mathrm{d}u_{ze1}}{\mathrm{d}z} + \frac{T_{e0}}{m_e n_0}\frac{\mathrm{d}n_1}{\mathrm{d}z} - \frac{e}{m_e}\frac{\mathrm{d}\phi_1}{\mathrm{d}z} + \frac{1}{m_e}\frac{\mathrm{d}T_{e1}}{\mathrm{d}z} = \left(i\omega - ik_y u_{ye0} - \frac{\mathrm{d}u_{ze0}}{\mathrm{d}z} - \nu_{e0}\right)u_{ze1} + \\ + \frac{eB}{m_e}u_{ye1} + \frac{T_{e0}}{m_e n_0^2}\frac{\mathrm{d}n_0}{\mathrm{d}z}n_1 - \frac{1}{m_e n_0}\frac{\mathrm{d}n_0}{\mathrm{d}z}T_{e1} \equiv F_4 \end{aligned} \tag{8d}$$

$$\begin{aligned} u_{ze0}\frac{\mathrm{d}u_{ye1}}{\mathrm{d}z} = \left(i\omega - ik_y u_{ye0} - \nu_{e0}\right)u_{ye1} - \left(\frac{\mathrm{d}u_{ye0}}{\mathrm{d}z} + \frac{eB}{m_e}\right)u_{ze1} - \\ - ik_y\frac{T_{e0}}{m_e n_0}n_1 + ik_y\frac{e}{m_e}\phi_1 - ik_y\frac{1}{m_e}T_{e1} \end{aligned} \tag{8e}$$

$$\begin{aligned} \frac{3}{2}u_{ze0}T_{e0}\frac{\mathrm{d}n_1}{\mathrm{d}z} + \frac{3}{2}u_{ze0}n_0\frac{\mathrm{d}T_{e1}}{\mathrm{d}z} + \frac{5}{2}n_0 T_{e0}\frac{\mathrm{d}u_{ze1}}{\mathrm{d}z} + \frac{\mathrm{d}q_{ze1}}{\mathrm{d}z} = \left(i\omega\frac{3}{2}T_{e0} - ik_y\frac{3}{2}u_{ye0}T_{e0} - \right. \\ \left. - \frac{3}{2}u_{ze0}\frac{\mathrm{d}T_{e0}}{\mathrm{d}z} - \frac{5}{2}T_{e0}\frac{\mathrm{d}u_{ze0}}{\mathrm{d}z} - \nu_{i0}E'_{i0} - \nu_{we0}T_{e0} + m_e\nu_{e0}u_{ye0}^2\right)n_{e1} + \\ + \left(-\frac{3}{2}\frac{\mathrm{d}n_0 T_{e0}}{\mathrm{d}z} + 2m_e\nu_{e0}n_0 u_{ze0}\right)u_{ze1} + \left(-ik_y\frac{5}{2}n_0 T_{e0} + 2m_e\nu_{e0}n_0 u_{ye0}\right)u_{ye1} + \\ + \left(i\omega\frac{3}{2}n_0 - ik_y\frac{3}{2}n_0 u_{ye0} - \frac{3}{2}u_{ze0}\frac{\mathrm{d}n_0}{\mathrm{d}z} - \frac{5}{2}n_0\frac{\mathrm{d}u_{ze0}}{\mathrm{d}z} - \nu_{we0}n_0 - \frac{5}{2}\frac{n_0 T_{e0}}{m_e\nu_{e0}}k_y^2\right)T_{e1} + \\ + ik_y\chi_0 q_{ze1} \end{aligned} \tag{8f}$$

$$\frac{5}{2}n_0 T_{e0}\frac{\mathrm{d}T_{e1}}{\mathrm{d}z} = -\frac{5}{2}T_{e0}\frac{\mathrm{d}T_{e0}}{\mathrm{d}z}n_1 - \frac{5}{2}n_0 T_{e0}\left(\frac{1}{T_{e0}}\frac{\mathrm{d}T_{e0}}{\mathrm{d}z} + ik_y\chi_0\right)T_{e1} - m_e\nu_{e0}\chi_0^2 q_{ze1} \equiv F_7 \tag{8g}$$

where ionization and wall source terms are neglected in the continuity and momentum equations and $1 + \chi_0^2 \approx \chi_0^2$ holds, being $\chi_0 = \omega_{ce}/\nu_{e0}$ the Hall parameter and $\omega_{ce} = eB/m_e$ the electron gyrofrequency. Ionization and wall interaction. The azimuthal component of the heat flow perturbation

$$q_{ye1} = -ik_y\frac{5}{2}\frac{n_0 T_{e0}}{m_e\nu_{e0}}T_{e1} - \chi_0 q_{ze1} \tag{9}$$

coming from Eq. (3f) projected along this direction, was conveniently substituted in order to reduce the computational cost of solving the stability problem. The inertia of electrons is not included in the first order electron heat flow, for simplicity. A fully consistent model requires to keep these terms, provided that they are not neglected in the electron momentum equation. This can be done as future work.

The system of first order fluid equations written in the form of Eqs. (8) hides the role played by sonic points in the model. From Eqs. (8a), (8b), (8c), (8d) and (8g), an equation involving only

the first order axial gradient of u_{zi1} can be derived

$$n_0\left(T_{e0}-m_iu_{zi0}^2-m_eu_{ze0}^2\right)\frac{\mathrm{d}u_{zi1}}{\mathrm{d}z}=m_eu_{ze0}u_{zi0}F_3- \\ -n_0u_{zi0}\left(m_iF_2+m_eF_4-\frac{2}{5}\frac{F_7}{n_0T_{e0}}\right)+\left(T_{e0}-m_eu_{ze0}^2\right)F_1\equiv G_1 \tag{10}$$

where we note that $m_eu_{ze0}^2 \ll m_iu_{zi0}^2$. This expression makes clearer the relevance of sonic points, where $T_{e0}=m_iu_{zi0}^2$ and there is a zero factor multiplying $\mathrm{d}u_{zi1}/\mathrm{d}z$ that may lead to singularities depending on the value of the right-hand side (G_1). Although the interior sonic point of the perturbed plasma moves with respect to the zeroth order position[22] (and this displacement can be computed as a post-processed result), we should only care about the zeroth order one for the application of the regularizing boundary condition. Similarly to the zeroth-order case[20] , the first order problem solved here has two sonic points of different type:

1. At the interior of the quasineutral plasma, where the zeroth-order ion flow undergoes a sonic transition. A continuous and smooth behaviour close to this point requires $G_{1S}=0$, which is a necessary boundary condition of the problem and makes possible for $\mathrm{d}u_{zi1}/\mathrm{d}z$ to take a finite value while still satisfying Eq. (10).
2. At the anode sheath edge, where ion velocity satisfy the Bohm condition. Here, the matching with the non-quasineutral sheath. Singularities are allowed at this boundary, where $G_{1B}\neq 0$ and, thus, the axial derivatives of perturbation variables tend to $\pm\infty$.

The boundary conditions follow closely those in Sec. IIA:

1. The perturbation on the total current at the cathode plane is zero, which yields

$$g_{c1}=e(u_{zi0N}-u_{ze0N})n_1+en_{0N}u_{zi1N}-en_{0N}u_{ze1N}=0 \tag{11}$$

2. For the perturbed solution to satisfy Bohm condition at B, it is required that

$$u_{zi1B}=-\frac{c_{s0B}}{2T_{e0B}}T_{e1B}=-\frac{1}{2m_ic_{s0B}}T_{e1B} \tag{12}$$

   Moreover, this condition is required in order to ensure the validity of the small perturbation assumption close to the anode singularity.[22] Numerical solutions of the first-order problem verify that, certainly, this is required to have moderate growth of perturbations at the anode boundary and good convergence behaviour with the number of grid points.

3. The perturbation potential at the anode wall (ϕ_{1A}) is zero. At the sheath edge the first order potential follows the linearized potential drop equation

$$e\phi_{1B}=\left(\frac{e\phi_{0AB}}{T_{e0B}}+\frac{1}{2}\right)T_{e1B}-\frac{T_{e0B}}{u_{ze0B}}u_{ze1B} \tag{13}$$

4. The heat flux matching condition and the sheath edge yields

$$q_{ze1B}=\left(e\phi_{0AB}-\frac{1}{2}T_{e0B}\right)u_{ze0B}n_{1B}+\left(e\phi_{0AB}-\frac{3}{2}T_{e0B}\right)n_{0B}u_{ze1B}+\frac{e\phi_{0AB}}{T_{e0B}}n_{0B}u_{ze0B}T_{e1B} \tag{14}$$

5. The temperature of injected electrons is assumed to be known and therefore $T_{e1N}=0$.
6. The azimuthal electron velocity perturbation is considered to be zero at the cathode axial position, i.e. $u_{ye1N}=0$. This condition is required in the first order problem because of keeping electron inertia effects. This is not the case of the integration of the zeroth order model, in which electron transport is diffusive and there are no axial gradients of u_{ye0} involved in the equations.
7. The regularizing boundary condition at point S required to ensure smooth behaviour close to the sonic point, i.e. $G_{1S}=0$.

The first order fluid equations and boundary conditions are homogeneous, reason why null perturbations are always a valid, but trivial, solution to the system. However, self-sustained oscillation (the eigenmodes of the problem) can still take place at specific values of the complex frequency ω (the eigenvalues), for given k_y and background solution. The real and imaginary parts of ω are the oscillation frequency (ω_r) and the growth rate (γ). Positive γ denotes a growing perturbation and, thus, an unstable behavior. The numerical method used to solve the frequencies and modal shapes of the perturbation problem is described in the Appendix A.

III. Results: without electron temperature perturbations

Stability is firstly investigated assuming null temperature perturbations. The system of equations to be solved comprises Eqs. (8a)-(8e) with $T_{e1} \approx 0$ and the corresponding boundary conditions. However, Eqs. (8f) and (8g) can still be used to make an estimate of T_{e1} and q_{ze1} in order to check if temperature perturbation terms are negligible in the electron momentum equation.

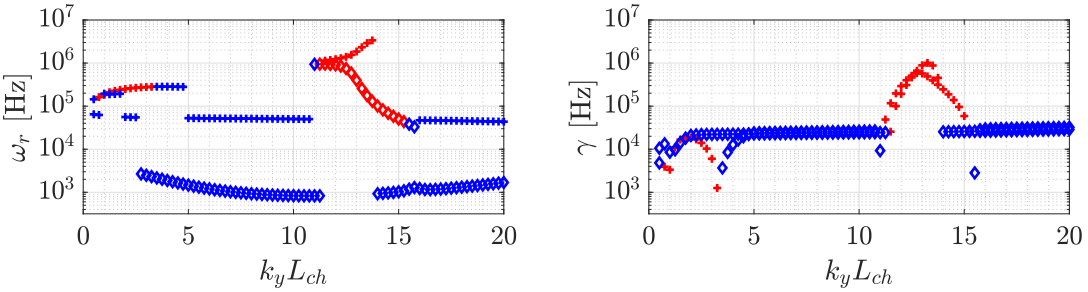

(a) Oscillation frequency **(b) Growth rate**

Figure 2: Global dispersion relations of the two most unstable modes, with $T_{e1} = 0$. Red and blue colours denote instability ($\gamma > 0$) and stable behavior ($\gamma < 0$), respectively. Diamond and cross markers account for negative and positive sign of the ordinate variable, respectively.

Fig. 2 shows ω_r and γ for the two most unstable modes at each $k_y L_{ch}$. Instabilities are found at two ranges of $k_y L_{ch}$ with clearly distinguished characteristics (outside from these ranges these modes become very stable and are difficult to track):

- $k_y L_{ch}$ within the range 0.75 to 3.25 (this is $\lambda_y \sim 21$ to 5 cm). The oscillations are concentrated in the subsonic region (see an example in Fig. 3). Only the perturbation potential shows significant oscillations in the supersonic ion flow.

  The values of ω_r fall in the medium-frequency band. This is, approximately, from 100 to 300 kHz. The azimuthal phase velocity ($u_{ph} = \omega_r / k_y$) of the waves is within the range 10-35 km/s, which is of the order of the background electron axial velocity close to the anode. The wave propagates in the $+\boldsymbol{E} \times \boldsymbol{B}$ direction.

  Comparing the relative orders of magnitude of the different terms in the electron momentum equation, we note that inertia terms are only important in the azimuthal direction and close to the anode (see Fig. 5a). Electron inertia is not a dominating effect but, even so, neglecting it makes this mode non-dominant (in terms of growth rate) and has significant effect on the evolution of the perturbations. Regarding electron pressure, neglecting it does not seem appropriate, as done in some similar works in the literature.[11–13] Finally, collisions play a negligible role in these modes.

  The features of this mode remind the close-anode gradient drift oscillations mentioned in the introduction and recently discussed in the literature.[8,9] On the other hand, close-anode oscillations with similar λ_y have been identified as rotating spoke instabilities[2] possibly enhancing electron transport in the close-anode region. The rotating spokes are measured, however, at rather lower frequencies ($\omega_r \sim$ 5-25 kHz) than those obtained by our calculations.

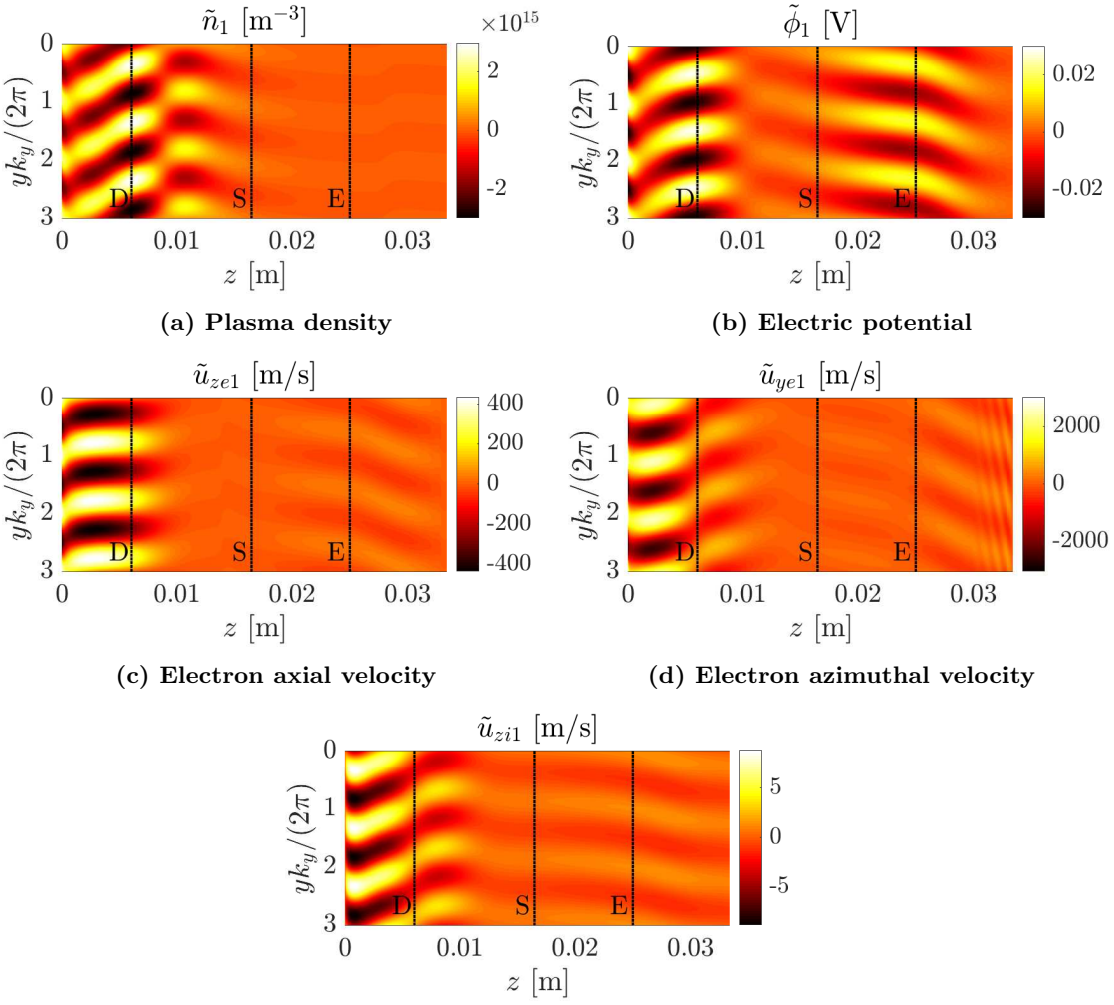

(a) Plasma density

(b) Electric potential

(c) Electron axial velocity

(d) Electron azimuthal velocity

(e) Ion axial velocity

Figure 3: Perturbation map in the axial-azimuthal plane, with $T_{e1} = 0$, for the most unstable mode at $k_y L_{ch} = 1.75$, with frequency 239 kHz. Perturbations scaled in order to get $\phi_1 = 30$ mV at the location of maximum module of the complex amplitude.

- $k_y L_{ch}$ within the range 11.25 to 13.75 (this is $\lambda_y \sim 1.4$ to 1.0 cm). In this case, the oscillations are found completely in the external part of the discharge (see an example in Fig. 4) and are mainly azimuthal, although some small amplitude fast axial waves are noticed (especially in $\tilde{u}_{ye1}$).

  The oscillation frequency ω_r is found to be of the order of 1-5 MHz, that is similar to the lower-hybrid frequency ω_{lh} at the exit. The azimuthal phase speed u_{ph} takes values in the range 10-40 km/s and modes in both $\pm \boldsymbol{E} \times B$ directions are found. This is close to u_{zi0} in the plume. Since the ion Mach number is, here, of the order of 10, u_{ph} is greater than c_{s0} by one order of magnitude.

  Looking at the different terms contributing to the electron momentum equation, the magnetic force seems to be mostly balanced by the electric force. However, electron inertia terms cannot be neglected since they are comparable to magnetic and electric forces in some small regions of the plume. It has been verified that neglecting them leads to a large impact in the evolution of perturbations. Electron pressure plays a secondary role (let us note that pressure fluctuations are only produced by n_1 since $T_{e1} = 0$ was assumed) and collisional terms are negligible.

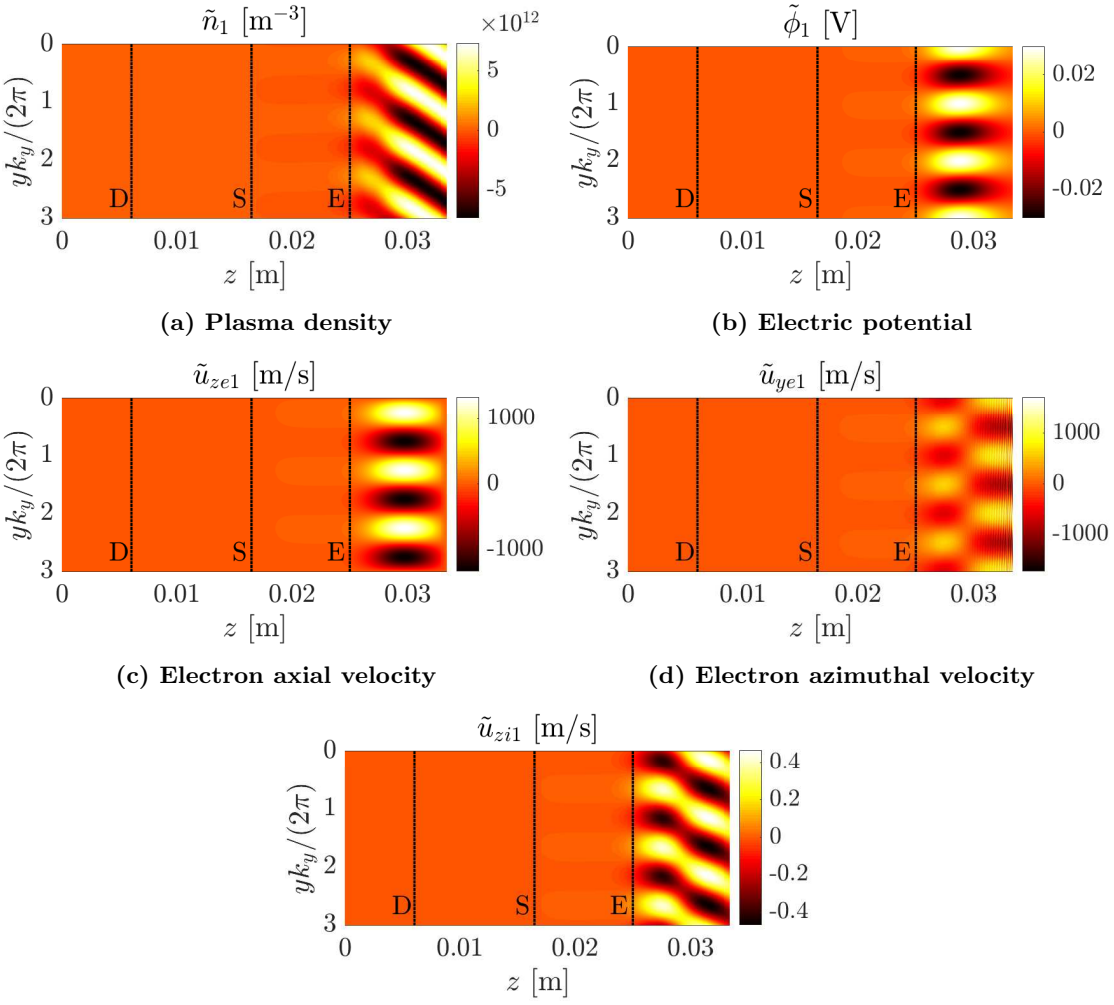

(a) Plasma density

(b) Electric potential

(c) Electron axial velocity

(d) Electron azimuthal velocity

(e) Ion axial velocity

Figure 4: Perturbation map in the axial-azimuthal plane, with $T_{e1} = 0$, for the most unstable mode at $k_y L_{ch} = 13.5$, with frequency 2.91 MHz. Perturbations scaled in order to get $\phi_1 = 30$ mV at the location of maximum module of the complex amplitude.

The oscillation frequency and location of the perturbations resemble to the characteristics of electron drift modes (introduced in Sec. I) although λ_y and u_{ph} take intermediate values between large and small-scale electron drift waves. Moreover, there are two unstable branches of modes in Fig. 2 corresponding to azimuthally counter-propagating modes with similar features to those aforementioned. This is also observed in ECDI empirical results in the literature.[23] Although there seems to be a connection between the modes shown here and electron drift waves at other scales, there is no experiment[10,16,23,24] or simulation[17,25] (to the best of our knowledge) that could appropriately reproduce or refute the modes computed with our model (in some cases due to insufficient k_y-spectrum resolution).

Under the obtained results, it is still not clear if fluid models capture the physics required to see instabilities at scales of the electron Larmor radius ℓ_e. Nevertheless, our analysis predicts instabilities in the centimeter range (this is at scales one-order-of-magnitude smaller than the thruster circumference), which is an advance towards such small scales, with respect to other global macroscopic perturbation works.[13] Let us remark that there are some effects missing in our model that could be non-negligible at ℓ_e and sub-ℓ_e scales, e.g., non-neutral or gyroviscous effects. Moreover, it was assumed that $T_{e1} = 0$, which is undone in the next

section.

The first order model described in Sec. IIB assumes quasineutral plasma perturbations. Once results have been obtained, the level of compliance of the solution with this assumption can be assessed. This is done using first-order Poisson equation in order to estimate the difference between ion and electron densities from the Laplacian of the potential perturbation. Provided that this difference ($n_{i1} - n_{e1}$) is much smaller than the quasineutral result for the plasma density (n_{1QN}), the quasineutral approximation is expected to provide accurate results. Results, for the examples in Fig. 3 and 4, are shown in Fig. 6 and reveal that the obtained modes can be approximately considered quasineutral.

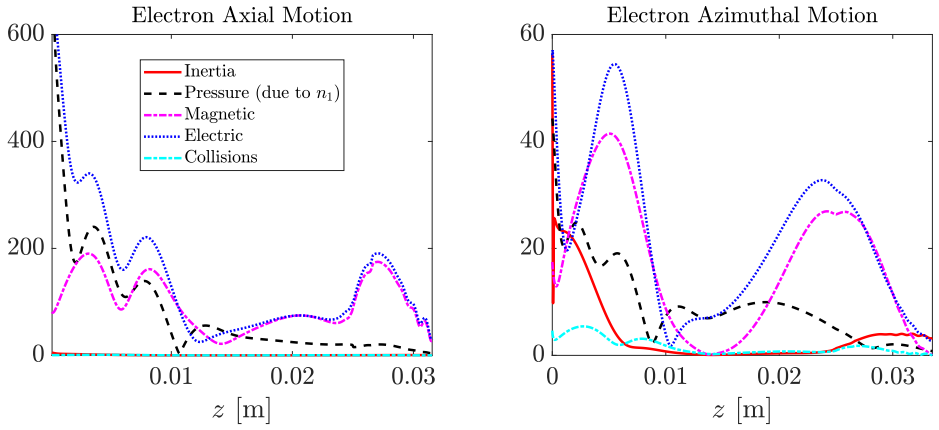

(a) $k_y L_{ch} = 1.75$ **and** $\omega_r = 239$ **kHz. See Fig. 3.**

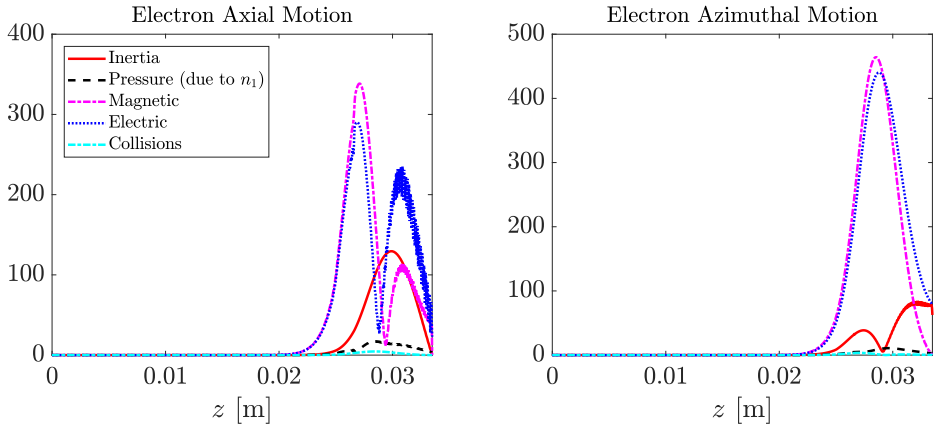

(b) $k_y L_{ch} = 13.5$ **and** $\omega_r = 2.91$ **MHz. See Fig. 4.**

Figure 5: Absolute values of the terms in the first order axial and azimuthal electron motion equations (Eqs. (8d) **and** (8e)**, respectively), with** $T_{e1} = 0$**, scaled with** $\nu_{\text{ref}} c_{\text{ref}}/\mu$**, being** $\nu_{\text{ref}} = 9.83 \times 10^4$ **s**$^{-1}$**,** $c_{\text{ref}} = 2.97$ **km/s and** $\mu = \sqrt[4]{m_e/m_i} = 0.0451$**.**

A. Parametric dependence

In this section the global stability calculations are repeated for different background plasma solutions, corresponding to parametric variations with respect to the nominal case in Table 2. The maximum amplitude of the magnetic field is modified accordingly with other parameters in order to keep optimum thruster operation.[26] Three parameters are varied:

- The discharge voltage (V_d). Instabilities within the frequency range 1-10 MHz at scales $k_y L_{ch} \sim 9 - 14$ ($\lambda_y \sim$ 1.1-1.7 cm for nominal L_{ch}) are found in every case with oscillations in the near plume, as Fig. 4, and growing values of ω_r with V_d. This response of the frequency to increasing V_d has been observed empirically in high frequency oscillations in Hall thrusters.[27]

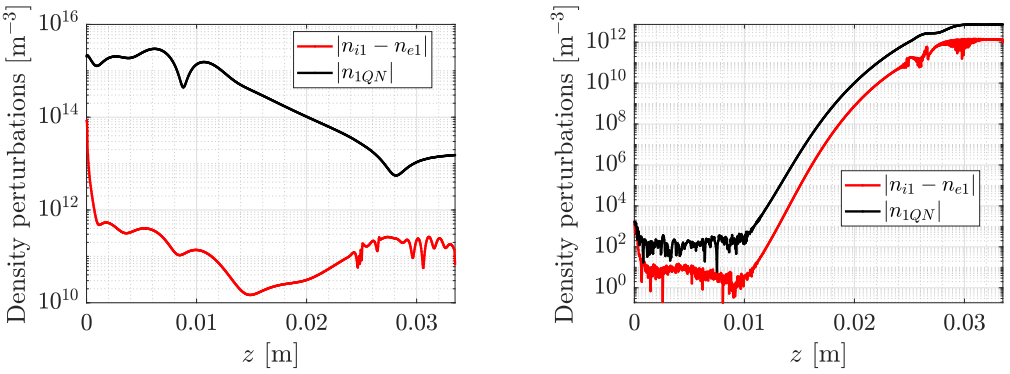

(a) $k_y L_{ch} = 1.75$ **and** $\omega_r = 239$ **kHz. See Fig. 3.**

(b) $k_y L_{ch} = 13.5$ **and** $\omega_r = 2.91$ **MHz. See Fig. 4.**

Figure 6: Validity of the quasineutral perturbation assumption for solutions with $T_{e1} = 0$**.**

Regarding the near-anode instabilities found, in the nominal case, at larger scales (see and example in Fig. 3), they are not found in the case $V_d = 700$ V but are present for $V_d = 200$ V in a very narrow $k_y L_{ch}$ range in Fig. 7b. Also for these modes, ω_r increases with V_d. These two features resemble the rotating spoke instabilities, as reported in the literature.[28]

- The channel length (L_{ch}). This parameter seem to have a greater impact on the frequency spectrum (see Fig. 8). High-frequency oscillations in the near plume are found for every parametric case within similar scales. For the case $L_{ch} = 1.4$ cm, analogous modes also appear at larger scales $k_y L_{ch} \sim 0.5 - 6$ ($\lambda_y \sim 1.4$-18 cm for $L_{ch} = 1.4$). These high-frequency large scale modes fit with the characteristic of electron drift modes at scales of the thruster circumference.[13]

  If the channel length is increased ($L_{ch} = 5.5$ cm), near-anode modes become dominant at scales $k_y L_{ch} < 8$ ($\lambda_y > 4.3$ cm for $L_{ch} = 5.5$ cm) with $\omega_r \sim 35 - 62$ kHz. These frequencies are closer to those typically associated to rotating spokes. Moreover, rotating spokes were observed in a long-channel (10 cm) thruster[2] for the first time and PIC simulations[29] suggest that they appear if the anode-cathode distance is large enough.

  Also in the case $L_{ch} = 5.5$ cm, new unstable modes appear at the smallest studied scales with $\omega_r \sim \omega_{ce} \sim 800$ MHz and $u_{ph} \sim c_{e0} \sim 1,600$ km/s. These modes are characterised by oscillations in the near-plume region and diminished n_1 and u_{zi1}. Because plasma density perturbations are small compared to other variables, the first-order solution highly violates quasineutrality and these modes are not reliable.

- Anode mass flow rate ($\dot{m}_A$). The main difference with respect to the nominal parametric case is that close-anode modes are unstable within a wider range of scales, i.e., for $\lambda_y > 1.6$ cm. Although ω_r shows a general drop, oscillation frequencies remain close to 100 kHz.

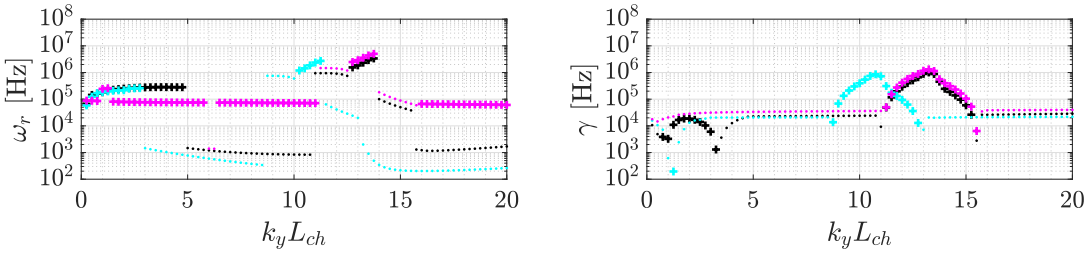

(a) Oscillation frequency **(b) Growth rate**

Figure 7: Global dispersion relations of the most unstable mode, with $T_{e1} = 0$ and the parametric cases: $V_d = 200$ V, $B_{max} = 179$ G (cyan); $V_d = 700$ V, $B_{max} = 383$ G (magenta) and nominal $V_d = 300$ V, $B_{max} = 251$ G (black). Dot and cross markers account for negative and positive sign of the ordinate variable, respectively.

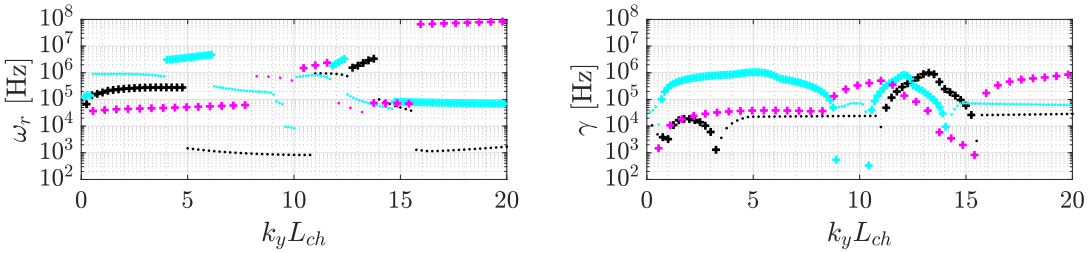

(a) Oscillation frequency **(b) Growth rate**

Figure 8: Global dispersion relations of the most unstable mode, with $T_{e1} = 0$ and the parametric cases: $L_{ch} = 1.4$ cm, $B_{max} = 401$ G (cyan); $L_{ch} = 5.5$ cm, $B_{max} = 383$ G (magenta) and nominal $L_{ch} = 2.5$ cm, $B_{max} = 251$ G (black). Dot and cross markers account for negative and positive sign of the ordinate variable, respectively.

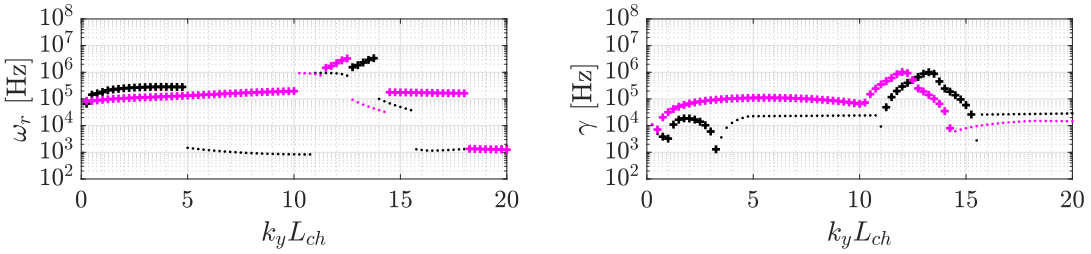

(a) Oscillation frequency **(b) Growth rate**

Figure 9: Global dispersion relations of the most unstable mode, with $T_{e1} = 0$ and the parametric cases: $\dot{m}_A = 8.5$ mg/s, $B_{max} = 249$ G (magenta) and nominal $\dot{m}_A = 4.75$ mg/s, $B_{max} = 251$ G (black). Dot and cross markers account for negative and positive sign of the ordinate variable, respectively.

B. Cross-field electron transport

The net axial long-term impact of perturbations in the electron transport is assessed with the azimuthal electron momentum equation averaged over one wave period and one azimuthal wavelength. If plasma variables are still expressed as in Eq. (1), the averaging operation cancels

firs-order terms out, yielding

$$m_e \left\langle \tilde{n}_1 \frac{\partial \tilde{u}_{ye1}}{\partial t} \right\rangle + m_e n_0 \left\langle \tilde{u}_{ze1} \frac{\partial \tilde{u}_{ye1}}{\partial z} \right\rangle + m_e u_{ze0} \left\langle \tilde{n}_1 \frac{\partial \tilde{u}_{ye1}}{\partial z} \right\rangle +$$
$$+ m_e \frac{\partial \tilde{u}_{ye0}}{\partial z} \langle \tilde{n}_1 \tilde{u}_{ze1} \rangle + m_e n_0 \left\langle \tilde{u}_{ye1} \frac{\partial \tilde{u}_{ye1}}{\partial y} \right\rangle + m_e u_{ye0} \left\langle \tilde{n}_{e1} \frac{\partial \tilde{u}_{ye1}}{\partial y} \right\rangle =$$
$$= - \left\langle \frac{\partial}{\partial y} \left(\tilde{n}_1 \tilde{T}_{e1} \right) \right\rangle - e \langle \tilde{n}_1 \tilde{E}_{y1} \rangle - eBn_0 u_{ze0} \tag{15}$$

where the angle brackets denote the averaging operator, electrons collisions were neglected (this is expected in regions where transport is mainly driven by turbulence) and the second order magnetic force is neglected against the zeroth order part. The zeroth-order electron inertia is neglected also against the magnetic force, although some comments will be made concerning this matter. The previous equation can be expressed as

$$F_{yt} - eBn_0 u_{ze0} = 0 \tag{16}$$

in which all averaged quadratic terms were condensed into an equivalent azimuthal force (F_{yt}), that balances out the magnetic force produced by the axial electron current. This expression highlights how quadratic terms impact the axial electron transport. But it also reveals that $u_{ze0} > 0$ is required whenever $F_{yt} > 0$, which is unconventional in Hall thrusters and can be observed to happen in Fig. 10.

The zeroth-order electron inertia is neglected in Eq. (15) and in the model used for background solutions.[19] This is justified as long as $\mathrm{d}u_{ye0}/\mathrm{d}z \ll \omega_{ce}$, that may fail close to the anode and in the plume. Thus, the zeroth-order electron inertia could contribute to the anomalous transport[21] and correct the sign of F_{yt}.

The anomalous electron transport due to plasma oscillations is typically explained in the literature using the quadratic term $e\langle \tilde{n}_1 \tilde{E}_{y1} \rangle$ in Eq. (15). However, we show here the existence of other quadratic terms, coming from electron inertia and electron pressure, that could also enhance cross-field transport. We find that the inertia contribution can be of the same order than the electrostatic one (see Fig. 10), in the two types of instabilities introduced previously in this section.

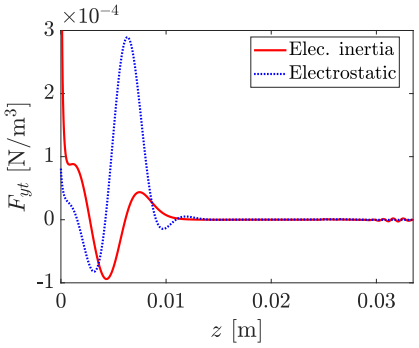

(a) $k_y L_{ch} = 1.75$ **and** $\omega_r = 239$ **kHz. See Fig. 3**

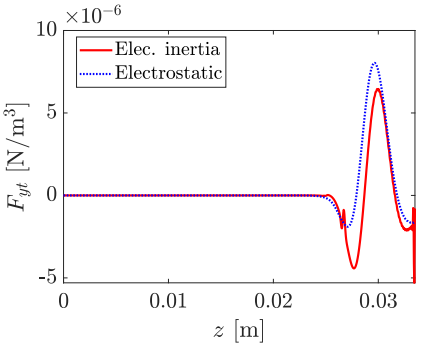

(b) $k_y L_{ch} = 13.5$ **and** $\omega_r = 2.91$ **MHz. See Fig. 4**

Figure 10: Second order contributions to the average cross-field electron transport expressed as an equivalent azimuthal force F_{yt}.

C. Comparison with local stability results

Here we try to establish a connection between the wave modes obtained with global and local approaches. Local dispersion relations are firstly derived for a specific assumed ordering (let us

remind that the axial-gradient operator applied to forst order variables is ik_z). For the background, we assume that

$$u_{zi0} \sim u_{ze0} \sim c_{s0} \quad u_{ye0} \sim \frac{c_{s0}}{\mu} \sim c_{e0}\mu \quad e\phi_0 \sim T_{e0} = m_i c_{s0}^2 \quad \nu_{e0} \sim \omega_{ce}\mu \quad \frac{\mathrm{d}}{\mathrm{d}z} \sim \frac{\mu}{\ell_{e0}} \tag{17}$$

being $c_{s0} = \sqrt{T_{e0}/m_i} \sim 3 \times 10^3$ m/s the ion sonic speed, $c_{e0} = \sqrt{8T_{e0}/(\pi m_e)} \sim 2.5 \times 10^6$ m/s the electron thermal speed, $\mu = \sqrt[4]{m_e/m_i} \approx 0.0451$ for Xenon as propellant, $\omega_{ce} = eB/m_e \sim 0.4$ GHz the electron cyclotron frequency and $\ell_{e0} \sim c_{e0}/\omega_{ce} \sim 2$ mm the electron Larmor radius. On the other hand, wave properties and perturbations are assumed to obey

$$\omega \sim \omega_{ce}\mu \qquad k_z \sim \frac{\omega}{c_{s0}} \sim \frac{1}{\mu \ell_{e0}} \qquad k_y \sim \frac{\omega}{u_{ye0}} \sim \frac{1}{\ell_{e0}} \tag{18}$$

and

$$\frac{u_{ye1}}{u_{ye0}} \sim \frac{u_{ze1}}{c_{s0}} \sim \varepsilon \qquad \frac{u_{zi1}}{c_{s0}} \sim \frac{n_1}{n_0} \sim \frac{e\phi_1}{T_{e0}} \sim \varepsilon\mu^2 \tag{19}$$

respectively; with ε being an arbitrary scaling parameter for the perturbations. Keeping only the dominant terms in Eqs. (8a)-(8f) yields

$$k_z u_{zi0} n_1 + k_z n_0 u_{zi1} = \omega n_1 \tag{20a}$$

$$k_z m_i u_{zi0} u_{zi1} + k_z e\phi_1 = \omega m_i u_{zi1} \tag{20b}$$

$$k_z u_{ze1} = -k_y u_{ye1} \tag{20c}$$

$$k_z \frac{T_{e0}}{n_0} n_1 - k_z e\phi_1 = -ieB u_{ye1} \tag{20d}$$

$$k_z m_e u_{ze0} u_{ye1} = (\omega - k_y u_{ye0} + i\nu_e)\, m_e u_{ye1} - k_y \frac{T_{e0}}{n_0} n_1 + k_y e\phi_1 + ieB u_{ze1} \tag{20e}$$

The values of ω that allow non-trivial solutions to these equations are

$$\omega_{ia}^{\pm} = k_z \left(u_{zi0} \pm c_{s0}\right) \tag{21}$$

$$\omega_{ed} = k_y u_{ye0} + k_z u_{ze0} - i\nu_{e0} \tag{22}$$

The modes with $\omega_{ia}^{\pm}$ are critically stable and propagate with axial phase speed $u_{zi0} \pm c_{s0}$ and, thus, can be identified as *ion acoustic* waves. They propagate in opposite directions in the subsonic region, while they can only move downstream in the supersonic part of the discharge. On the other hand, the mode with ω_{ed} is associated to the drift motion of electrons (both azimuthal and axial) and is damped by collisions. For oblique waves ($|k_y| \sim |k_z|$) and azimuthal waves ($|k_y| > |k_z|$), ω_{ed} is approximately independent of k_z, since $|u_{ye0}| \gg |u_{ze0}|$ within the whole domain. Let us emphasize that the employed ordering leads to equations without zeroth-order axial gradients, which usually play a role in local instability criteria.[9,30,31] Furthermore, the magnetic field is not involved in these modes because Eqs. (20c) and (20d) imply a balance of pressure and electromagnetic forces in the azimuthal direction.

The ordering assumed in order to derive the previous expressions is not completely coherent with the results of the global analysis and it is unable to predict any instability. Even so, complex frequencies of local modes computed numerically (see Appendix A) with a more complicated model (e.g. Eqs. (8a)-(8f)) are easy to correlate with either $\omega_{ia}^{\pm}$ or ω_{ed} (see Figs. 11 and 12). This result suggests that Eqs. (21) and (22) properly capture some fundamental characteristics of the local modes obtained with more complete models.

In Figs. 11 and 12, the cases $k_y \sim \pm k_z$ is considered (for one specific example with $k_y L_{ch} = 12.5$), because these seem to be dominant contributions to the k_z-spectrum in global solutions (examples in Figs. 4 and 3). The numerical result, as well as the analytical one, shows a change in the sign of $\mathrm{Re}\{\omega_{ia}^{\pm}\}$ with the sign of $k_z L_{ch}$; while $\mathrm{Re}\{\omega_{ed}\}$ is nearly independent of $k_z L_{ch}$. Moreover,

the analytical expressions are fairly accurate close to the anode and to the cathode. At the exit $\mathrm{Re}\{\omega_{ia}^{\pm}\} \sim \pm 1.5$ MHz, which is of the order of the aforementioned modes with oscillations in the near plume (see Figs. 2 and 4). The value of $\mathrm{Re}\{\omega_{ia}^{\pm}\}$ moves to lower frequencies when closer to the anode ($\mathrm{Re}\{\omega_{ia}^{\pm}\} \sim \pm 100$ kHz close to point D), within the range of those unstable global modes with oscillations in the subsonic region (see Figs. 2 and 3). The frequencies of unstable modes, computed with a global approach, are, in every case, closer to those of ion-acoustic-like local modes.

Regarding the ability of local analyses to predict instability, the numerical results show $\gamma > 0$ for ion-acoustic-like mode in the subsonic region (independently of the sign of k_z), which is coherent with some of the obtained global modes. Regarding instabilities in the near plume region, they are shown in Fig. 12b when the signs of k_y and k_z differ. Nevertheless, it is the local mode associated to the electron drift motion that become unstable, whose frequencies are significantly greater than 1-5 MHz.

Although we have tried to establish a connection between local and global analyses, this is not direct since inhomogeneities in Hall thrusters and the effect of boundary conditions are not covered by local analyses. This fact has been already reported in the literature.[6] Moreover, adding k_z increases the dimension of the parametric space and makes the stability analysis difficult and not directly comparable to global results (where a discrete and large number of k_z, within an interval given by the grid refinement, is studied at the same time).

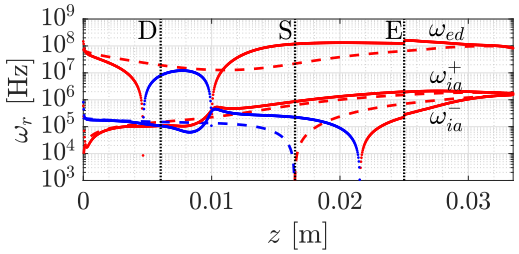

(a) Oscillation frequency

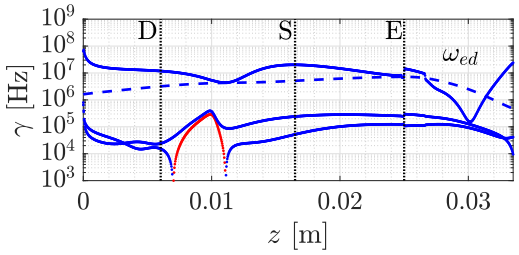

(b) Growth rate

Figure 11: Local dispersion relations for $k_y L_{ch} = k_z L_{ch} = 12.5$ computed numerically with Eqs. (8a)-(8f) (solid line) and analytically from Eqs. (21) and (22) (broken line). Red and blue colors denote positive and negative signs, respectively.

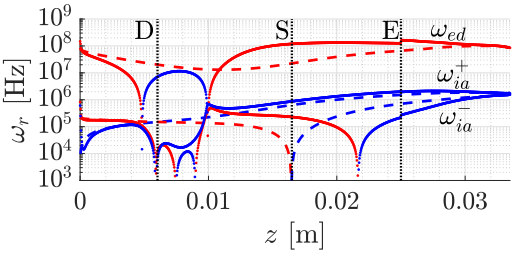

(a) Oscillation frequency

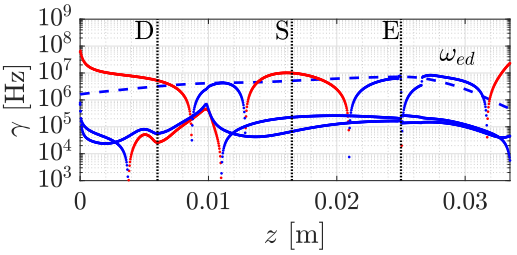

(b) Growth rate

Figure 12: Local dispersion relations for $k_y L_{ch} = -k_z L_{ch} = 12.5$ computed numerically with Eqs. (8a)-(8f) (solid line) and analytically from Eqs. (21) and (22) (broken line). Red and blue colors denote positive and negative signs, respectively.

IV. Results: with electron temperature perturbations

In this section, electron temperature perturbations are allowed ($T_{e1} \neq 0$). The system of equations to be solved comprises Eqs. (8) and the corresponding boundary conditions. This system includes two new variables, i.e. T_{e1} and q_{ze1}, with respect to the model used in the previous section.

The dispersion relation for the most unstable mode (with nominal parameters) at each $k_y L_{ch}$ is

displayed in Fig. 13 in magenta. The eigenvalues of the case with $T_{e1} = 0$ are also plotted in black, for comparison. Let us remark that, in contrast to Fig. 2, instabilities can be identified with cross markers in Fig. 13b.

Looking at Fig. 13b, we observe that the two unstable regions of the k_y-spectrum found with $T_{e1} = 0$ broaden in the case with $T_{e1} \neq 0$. Unstable modes are consequently found in the complete range of studied $k_y L_{ch}$. Nevertheless, the unstable modes found now are noted to be modifications of those observed with $T_{e1} = 0$:

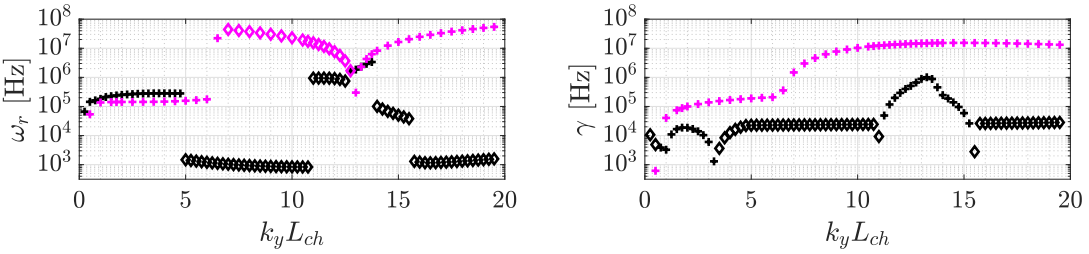

(a) Oscillation frequency **(b) Growth rate**

Figure 13: Global dispersion relations of the most unstable mode, comparing the results for $T_{e1} = 0$ (black) and $T_{e1} \neq 0$ (magenta). Diamond and cross markers account for negative and positive sign of the ordinate variable, respectively. The unstable character of the modes is determined solely by the sign of γ in the (b) panel.

- For $k_y L_{ch} \leq 6$ (this is $\lambda_y \geq 2.6$ cm) the unstable modes concentrate the oscillation in the near-anode subsonic region and ω_r take values between 50 and 180 kHz. Modes with very similar characteristics were found with $T_{e1} = 0$ at slightly higher frequencies. Even though pressure perturbations due to T_{e1} are not completely negligible, the first order Lorentz force and pressure oscillations due to n_1 are greater in the close-anode region. This fact would explain why, when neglecting the pressure term involving T_{e1}, some of the main features of these modes are recovered.

  The perturbation maps, quasineutrality check and azimuthal equivalent force look very similar to those in Figs. 3, 6a and 10a, respectively. There is, however, a non-negligible contribution to F_{yt} from pressure terms in Eq.(15).

  Including the temperature calculation in the perturbation model seems to lower the oscillation frequency of these modes. This result may reinforce the idea that they are a manifestation of the well-known rotating spokes. Since we are moving towards lower frequencies, some of the assumption done initially should be reconsidered.

- For $k_y L_{ch} \geq 6$ (this is $\lambda_y \leq 2.6$ cm) unstable modes are found with oscillations taking place in the near plume (see Fig. 14). The values of ω_r range (in absolute value) from 1 to 60 MHz. However, in the vicinity of $k_y L_{ch} = 13$, the values of ω_r there is a good matching with the dominant modes when $T_{e1} = 0$. These evidences suggest that the modes obtained with $T_{e1} \neq 0$ are a modified version of those explained with $T_{e1} = 0$. In the case $T_{e1} \neq 0$, these modes are unstable within a broader region of the k_y-spectrum and, thus, they are able to evolve towards larger frequencies (but still relatively close to typical values of electron drift modes).

  Despite the aforementioned similarities between both models, considering T_{e1} introduces important differences because pressure oscillations due to T_{e1} become one of the dominant terms in the electron momentum equation (see Fig. 17). Namely, the axial wavelengths of $\tilde{n}_1$, $\tilde{\phi}_1$ and $\tilde{u}_{zi1}$ become shorter; the maximum amplitudes of $\tilde{u}_{ze1}$ and $\tilde{u}_{ye1}$ increase by a factor of 2; and the amplitude of $\tilde{n}_1$ decrease by one order of magnitude[b] (compare Figs. 4 and 14). As consequences from the last point, inertia terms dominates over pressure and electrostatic

[b] Remind that the magnitude of the perturbation is arbitrary and was chosen such that $\tilde{\phi}_1$ is bounded between $\pm 1 \times 10^{-4} V_d$.

contributions to electron transport (see Fig. 16), and the quasineutral approximation fails (see Fig. 15).

Under this result, it would be needed to have a model that allowed for non-neutral peturbations on ion and electron densities, with the computational domain going from point A to N (instead of from B to N). This is, however, not direct and lies beyond the scope of this work. It is difficult to keep consistency between a quasineutral zeroth order model and a non-neutral first order model, due to, e.g., the treatment of the anode sheath (assumed infinitely thin in the zeroth order problem) or the different definition of the sonic point (in a non-neutral model each species has its own sonic point at different locations).

Nevertheless, our results suggest that the effect of T_{e1} should be considered. Not only because the corresponding terms are not negligible in the electron momentum equation, but also because it seems to play a relevant role in terms of instability within a wide range of scales.

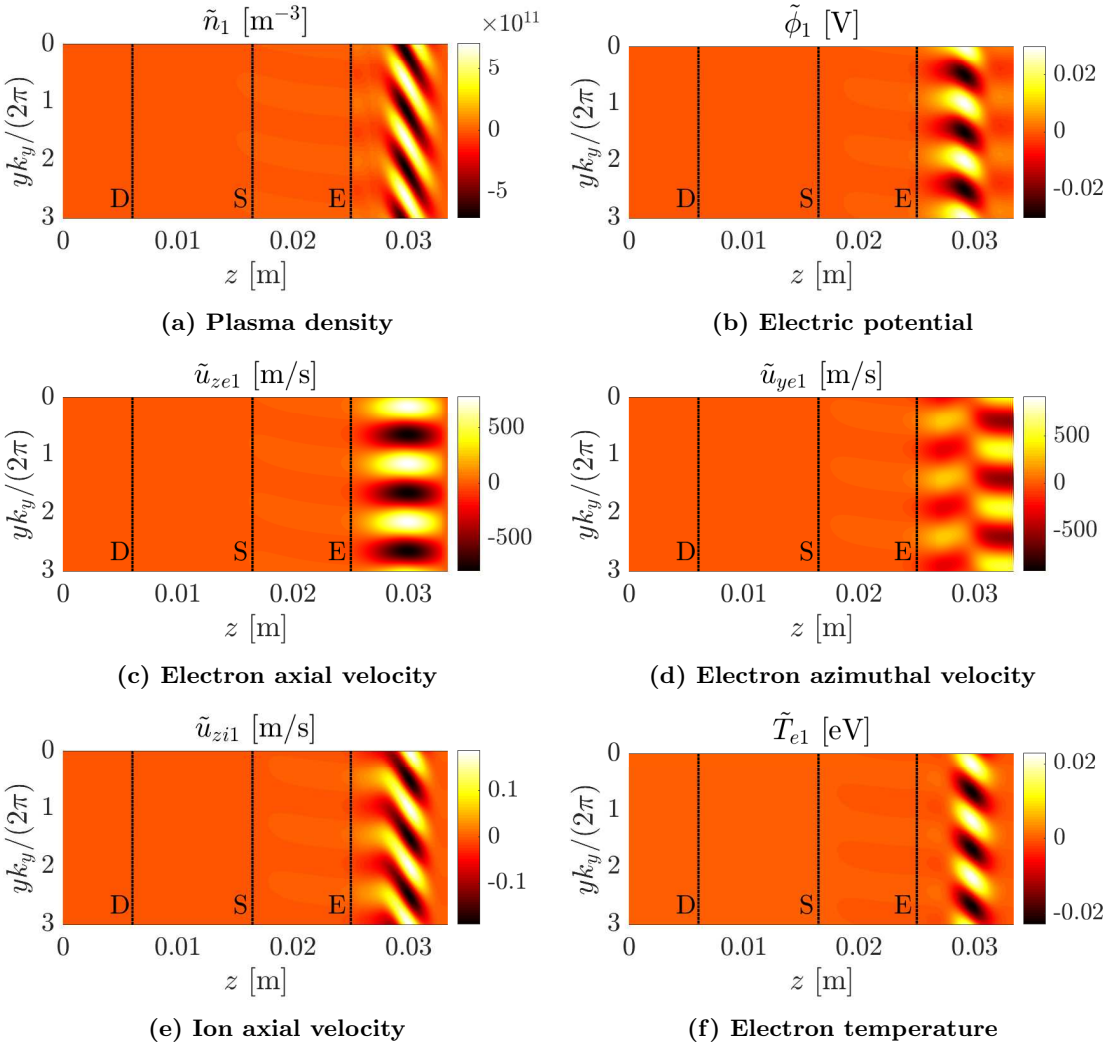

(a) Plasma density **(b) Electric potential**

(c) Electron axial velocity **(d) Electron azimuthal velocity**

(e) Ion axial velocity **(f) Electron temperature**

Figure 14: Perturbation map in the axial-azimuthal plane, with $T_{e1} \neq 0$, for the most unstable mode at $k_y L_{ch} = 13.5$, with frequency 4.28 MHz. Perturbations scaled in order to get $\phi_1 = 30$ mV at the location of maximum module of the complex amplitude.

V. Conclusion

High-frequency azimuthal oscillatory modes are studied in this work, for Hall thrusters, in the axial-azimuthal plane, using a global small perturbation approach and a macroscopic description

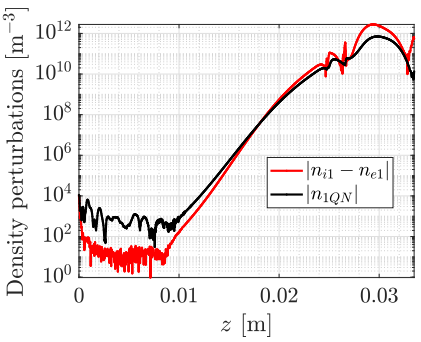

Figure 15: Quasineutral assumption validity on the most unstable mode, found with $T_{e1} \neq 0$ at $k_y L_{ch} = 13.5$ with $\omega_r = 4.28$ MHz.

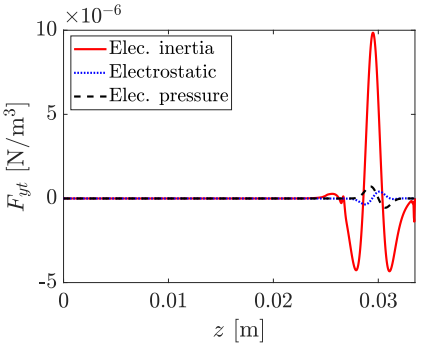

Figure 16: Impact on electron transport of the most unstable mode, found with $T_{e1} \neq 0$ at $k_y L_{ch} = 13.5$ with $\omega_r = 4.28$ MHz.

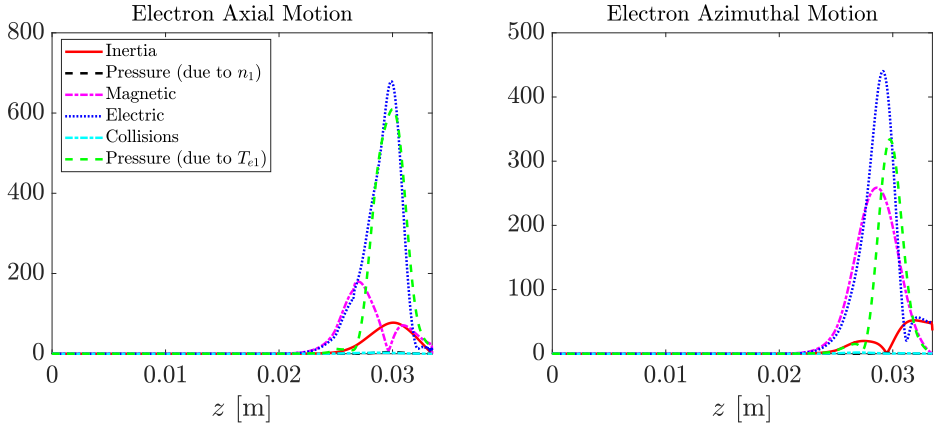

Figure 17: Absolute values of the terms in the first order axial and azimuthal electron motion equations (Eqs. (8d) and (8e), respectively), with $T_{e1} \neq 0$; scaled with $\nu_{\text{ref}} c_{\text{ref}}/\mu$, being $\nu_{\text{ref}} = 9.83 \times 10^4$ s^{-1}, $c_{\text{ref}} = 2.97$ km/s and $\mu = \sqrt[4]{m_e/m_i} = 0.0451$. The mode is the most unstable one for $k_y L_{ch} = 13.5$. See Fig. 14

for all plasma species. The background plasma solution is stationary and axisymmetric and the numerical method to compute it is well known.[19] The system of equations governing the perturbations, in the high-frequency regime, is introduced in Sec. IIB with the corresponding boundary conditions. After Fourier-transforming the first order variables in time and azimuthal coordinates, the resulting system of equations is of ordinary-differential type, with the axial coordinate being the independent variable. The solution to this problem yields the spectrum of complex frequencies and the corresponding complex-amplitude profiles for the first order variables, for given k_y and background plasma solution. A numerical method to solve this type of problems is proposed in Appendix A.

Initially, first-order effects from electron temperature are neglected, as it is typically done in other high-frequency analyses.[11–13] Two clearly distinguishable types of unstable modes are found at different azimuthal scales: (*i*) within $\lambda_y \sim$ 5-21 cm, $\omega_r \sim$ 100-300 kHz and characteristics in common with close-anode gradient drift[9] and rotating spoke[2] oscillations; and (*ii*) with $\lambda_y \sim 1$ cm, $\omega_r \sim$ 1-5 MHz and oscillations in the near plume, resembling electron drift modes at larger[10] and smaller[14] scales. When comparing these results with modes obtained from a local stability analysis, the range of frequencies $1 - 5$ MHz corresponds to ion-acoustic-like waves. Local modes associated to the electron drift motion have frequencies well beyond this band.

The effect of the electron temperature perturbations is noted to be far from negligible. Pressure fluctuations due to T_{e1} become one of the dominant terms in the electron momentum equation. Nevertheless, modified versions of the aforementioned instabilities can be identified, but occupying a broader range of azimuthal scales. Modes of type *i* are moved towards slightly smaller frequencies (50-180 kHz, which is closer to typical values of rotating spokes) but keeping the main properties already described. Modes of type *ii* have, in contrast, larger frequencies (1-60 MHz) and the values of plasma density perturbations decrease by one order of magnitude. As a consequence, the quasineutral assumption of the first-order model is violated. Even so, our results show that electron temperature effects cannot be disregarded and produce instabilities at large and small azimuthal scales.

Regarding the impact of plasma oscillations in cross-field electron transport, there is an electrostatic contribution from the correlation of azimuthal oscillations of plasma density and azimuthal electric field (the one that is typically considered), but we also suggest a possible non-negligible contribution from electron inertia and pressure terms. This is confirmed by our results.

A. Numerical method

The system of linearized macroscopic equations can be written as a general homogeneous system of ordinary differential equations

$$\bar{\mathbf{A}} \cdot \frac{\mathrm{d}\boldsymbol{x}_1}{\mathrm{d}z} = \left(\bar{\mathbf{B}} + i\omega\bar{\mathbf{C}} + ik_y\bar{\mathbf{D}} + k_y^2\bar{\mathbf{D}}_2\right) \cdot \boldsymbol{x}_1 \tag{23}$$

with $\boldsymbol{x}_1 = \boldsymbol{x}_1(z)$ being the vector first order variables and having length m (for the sake of generality); and the coefficients of matrices $\bar{\mathbf{A}}$, $\bar{\mathbf{B}}$, $\bar{\mathbf{C}}$, $\bar{\mathbf{D}}$ and $\bar{\mathbf{D}}_2$ being functions of z and $\boldsymbol{x}_0 = \boldsymbol{x}_0(z)$. Similarly, each boundary condition of the problem is homogeneous and can be expressed as a linear combination of the perturbation variables at the corresponding point of application (since our boundary conditions do not involve axial gradients).

Because of the first-order problem being homogeneous, a trivial solution is zero perturbation. However, for given k_y and background plasma state $\boldsymbol{x}_0(z)$, the problem also admits non-trivial solutions at specific values of the complex frequency ω. These values of ω and the corresponding complex perturbation profiles are the eigenvalues and eigenfunctions of the first order problem, respectively.

Solving the Eigen Boundary Value Problem (EBVP) described by Eq. (23) and boundary conditions takes in account global effects on stability, such as axial gradients and boundary conditions themselves. Alternatively, a local stability analysis takes the Fourier transform of the perturbations also in the axial direction, under which the axial gradient operator, applied to first order variables, becomes ik_z. The methods used to solve local and global linear stability of the Hall-thruster discharge are described in this appendix section.

Global stability

The system given by Eq. (23) is solved in a discrete way on an uniform grid with N points covering the distance from the anode sheath edge (B) to the cathode (N). The unknowns of the discrete problem ($\boldsymbol{X}_1$) are the values of the first order variables at the grid points. Let us use j as an index going from 1 to N to denote the position of points in the grid, with $j = 1$ corresponding to point B. This is a total of mN unknowns, which require of the same number of equations in order to solve the problem: m boundary conditions and $m\,(N-1)$ first order macroscopic equations. The $m\,(N-1)$ fluid equations come from evaluating each equation in system (23) in N different axial positions of the domain, which do not necessarily coincide with grid points. There are plenty of possibilities to proceed. Here, we will described the method that has been observed to have the most numerically robust behavior and that was used to obtain the presented results (some comments will be made on considered alternatives, highlighting the numerical difficulties found).

The proposed method evaluates the first order system (23) at intermediate points in between grid points (the non-integer index $j + 1/2$ denotes the midpoint between grid points j and $j + 1$). This

directly yields $m(N-1)$ equations, which can be written, analogously to Eq. (23), as the system

$$\bar{\mathbf{A}}_g \cdot \frac{\mathrm{d}\boldsymbol{X}_1^*}{\mathrm{d}z} = \left(\bar{\mathbf{B}}_g + i\omega\bar{\mathbf{C}}_g + ik_y\bar{\mathbf{D}}_g + k_y^2\bar{\mathbf{D}}_{2,g}\right) \cdot \boldsymbol{X}_1^* \tag{24}$$

where $\boldsymbol{X}_1^*$ stands for the vector of first order quantities at midpoints, which is $m(N-1)$ elements long. The matrices in the previous expression are squared with column length $m(N-1)$, and are global versions of those in Eq. (23). Their coefficients come from evaluating the local matrices at each midpoint. The specific arrangement of these coefficients within global matrices depends on the order used for the elements in vector $\boldsymbol{X}_1^*$.

Eq. (24) has to be expressed in terms of the unknown vector $\boldsymbol{X}_1$. In order to do so:

- The first-order derivatives at midpoints (collected in $\mathrm{d}\boldsymbol{X}_1^*/\mathrm{d}z$) are estimated, using grid-point values, with the centered finite difference formula

$$\left.\frac{\mathrm{d}\boldsymbol{x}_1}{\mathrm{d}z}\right|_{j+1/2} \approx \frac{\boldsymbol{x}_1^{j+1} - \boldsymbol{x}_1^j}{\Delta z} \tag{25}$$

  where Δz is the grid step. Using this equation it is possible to build a finite difference matrix $\bar{\mathbf{F}}$ such that

$$\frac{\mathrm{d}\boldsymbol{X}_1^*}{\mathrm{d}z} \approx \bar{\mathbf{F}} \cdot \boldsymbol{X}_1 \tag{26}$$

- The values of perturbations at midpoints (collected in $\boldsymbol{X}_1^*$) can be estimated as the mean of the values at the two nearest grid points, i.e

$$\boldsymbol{x}_1^{j+1/2} \approx \frac{\boldsymbol{x}_1^j + \boldsymbol{x}_1^{j+1}}{2} \tag{27}$$

  This expression can be used to build an averaging matrix $\bar{\mathbf{M}}$ such that $\boldsymbol{X}_1^* \approx \bar{\mathbf{M}} \cdot \boldsymbol{X}_1$

The size of matrices $\bar{\mathbf{F}}$ and $\bar{\mathbf{M}}$ is $m(N-1) \times mN$.

Using these two approximations in Eq. (24) yields

$$\bar{\mathbf{A}}_g \cdot \bar{\mathbf{F}} \cdot \boldsymbol{X}_1 = \left(\bar{\mathbf{B}}_g + i\omega\bar{\mathbf{C}}_g + ik_y\bar{\mathbf{D}}_g + k_y^2\bar{\mathbf{D}}_{2,g}\right) \cdot \bar{\mathbf{M}} \cdot \boldsymbol{X}_1 \tag{28}$$

This is an algebraic system of equations for $\boldsymbol{X}_1$ which must be completed, however, with the boundary conditions of the problem. This is evident when looking at the dimensions of the matrices in the previous expression (including the multiplication by $\bar{\mathbf{F}}$ and $\bar{\mathbf{M}}$ in the left and right-hand sides, respectively): $m(N-1) \times mN$.

The set of linear homogeneous boundary conditions of the problem can be expressed as linear combinations of the the discrete unknowns of the problem $\bar{\mathbf{G}} \cdot \boldsymbol{X}_1 = \mathbf{0}$. The complete discrete system of equations that gives an approximate solution to the EBVP of Eq. (23) reads

$$\left[\begin{pmatrix} \bar{\mathbf{A}}_g \cdot \bar{\mathbf{F}} - \left(\bar{\mathbf{B}}_g + ik_y\bar{\mathbf{D}}_g + k_y^2\bar{\mathbf{D}}_{2,g}\right) \cdot \bar{\mathbf{M}} \\ \bar{\mathbf{G}} \end{pmatrix} - \begin{pmatrix} \bar{\mathbf{C}} \cdot \bar{\mathbf{M}} \\ \bar{\mathbf{0}} \end{pmatrix} i\omega \right] \cdot \boldsymbol{X}_1 = \mathbf{0} \tag{29}$$

and has the form of a generalized algebraic eigenvalue problem with ω and the corresponding $\boldsymbol{X}_1$ being the eigenvalues and eigenvectors, respectively. By separating the eigenvector in each first order variable, the axial evolution of the perturbation complex amplitudes are obtained. This problem can be solved with several MATLAB routines (*eig*, *eigs* or *polyeig*). The method shows numerical convergence with the number of grid points and has been successfully verified with test EBVPs with analytical solution.

As aforementioned, alternative discretizations could be used. One possibility is to evaluate the first order fluid equations at grid points (instead of at midpoints) and use forward, centered and backward finite difference schemes for estimating axial gradients at left boundary, interior points and right boundary, respectively. However, the complete system (23) cannot be evaluated at every

grid point, since this provides mN equations before including boundary conditions in the count. Therefore, m fluid equations must be disregarded in order to make room for boundary conditions. It is not trivial to decide which discrete first order equations should be eliminated from the system. Moreover, this approach leads to the appearance of spurious normal modes, which is not observed if using a centered method. These differences in numerical behavior has been successfully identified in test EBVP with analytical solution.

Local stability

After applying the Fourier transform in the axial direction (assuming $1/k_z$ much larger than the characteristic length associated to background plasma gradients) and moving all terms to the right-hand side, Eq. (23) reads

$$\left(\bar{\mathbf{B}} + i\omega\bar{\mathbf{C}} + ik_y\bar{\mathbf{D}} + k_y^2\bar{\mathbf{D}}_2 - ik_z\bar{\mathbf{A}}\right)\cdot\boldsymbol{x}_1 = \mathbf{0} \tag{30}$$

which has the form of an algebraic eigenvalue problem of dimension m. The values of ω providing non-trivial solutions can be solved independently for each axial position. The same aforementioned MATLAB solvers can be used.

Acknowledgements

This work has received funding from the PROMETEO-CM project, Grant number Y2018/NMT-4750 (Comunidad de Madrid/FEDER/FSE). and from Project ESP2016-75887 (Spain's National Research and Development Plan - MINECO/FEDER).

References

[1]A.I. Morozov, Y.V. Esipchuk, G.N. Tilinin, A.V. Trofimov, Y.A. Sharov, and G.Y.Shchepkin. Plasma accelerator with closed electron drift and extended acceleration zone. *Soviet Physics-Tech. Physics*, 17(1):38–45, 1972.

[2]G.S. Janes and R.S. Lowder. Anomalous electron diffusion and ion acceleration in a low-density plasma. *Physics of Fluids*, 9(6):1115–1123, 1966.

[3]E. Choueiri. Plasma oscillations in Hall thrusters. *Physics of Plasmas*, 8(4):1411–1426, 2001.

[4]J.P. Boeuf and B Chaudhury. Rotating instability in low-temperature magnetized plasmas. *Phys. Rev. Lett.*, 111:155005, 2013.

[5]A.I. Smolyakov, O. Chapurin, W. Frias, O. Koshkarov, I. Romadanov, T. Tang, M. Umansky, Y. Raitses, I.D. Kaganovich, and V.P. Lakhin. Fluid theory and simulations of instabilities, turbulent transport and coherent structures in partially-magnetized plasmas of ExB discharges. *Plasma Physics and Controlled Fusion*, 59:014041, 2017.

[6]Diego Escobar and E. Ahedo. Low frequency azimuthal stability of the ionization region of the hall thruster discharge. ii. global analysis. *Physics of Plasmas*, 22:102114, 2015.

[7]N. Gascon and M.A. Cappelli. Plasma instabilities in the ionization regime of a Hall thruster. In *39th AIAA Joint Propulsion Conf*, page 2003, 2003.

[8]V. P. Lakhin, V. I. Ilgisonis, A. I. Smolyakov, E. A. Sorokina, and N. A. Marusov. Effects of finite electron temperature on gradient drift instabilities in partially magnetized plasmas. *Physics of Plasmas*, 25:012106, 2018.

[9]N A Marusov, E A Sorokina, V P Lakhin, V I Ilgisonis, and A I Smolyakov. Gradient-drift instability applied to hall thrusters. *Plasma Sources Science and Technology*, 28(1):015002, 2019.

[10]Y.V. Esipchuk and G.N. Tilinin. Drift instability in a Hall-current plasma accelerator. *Sov. Physics-Tech. Physics*, 21(4):417–423, 1976.

[11]A. Kapulkin, J. Ashkenazy, A. Kogan, G. Appelbaum, D. Alkalay, and M. Guelman. Electron instabilities in Hall thrusters: Modeling and application to electric field diagnostics. In *Proceedings of the 28th International Electric Propulsion Conference*, 2003.

[12]A.A. Litvak and N.J. Fisch. Rayleigh instability in Hall thrusters. *Physics of Plasmas*, 11:1379, 2004.

[13]Diego Escobar and E. Ahedo. Numerical analysis of high-frequency azimuthal oscillations in hall thrusters. In 34^{th} *International Electric Propulsion Conference*, number IEPC-2015-371, Hyogo-Kobe, Japan, July 6-10, 2015. Electric Rocket Propulsion Society.

[14]D.W. Forslund, R.L. Morse, and C.W. Nielson. Electron cyclotron drift instability. *Physical Review Letters*, 25:1266–1270, 1970.

[15]H.V. Wong. Electrostatic electron-ion streaming instability. *Physics of Fluids*, 13:757–760, 1970.

[16]S. Tsikata and T. Minea. Modulated electron cyclotron drift instability in a high-power pulsed magnetron discharge. *Physical Review Letters*, 114:185001, 2015.

[17]T. Lafleur, S.D. Baalrud, and P. Chabert. Theory for the anomalous electron transport in hall effect thrusters. i. insights from particle-in-cell simulations. *Physics of Plasmas*, 23:053502, 2016.

[18]T. Lafleur, S.D. Baalrud, and P. Chabert. Theory for the anomalous electron transport in hall effect thrusters. ii. kinetic model. *Physics of Plasmas*, 23:053503, 2016.

[19]E. Ahedo, J.M. Gallardo, and M. Martínez-Sánchez. Effects of the radial-plasma wall interaction on the axial Hall thruster discharge. *Physics of Plasmas*, 10(8):3397–3409, 2003.

[20]E. Ahedo, P. Martínez-Cerezo, and M. Martínez-Sánchez. One-dimensional model of the plasma flow in a Hall thruster. *Physics of Plasmas*, 8:3058–3068, 2001.

[21]E. Ahedo, J.M. Gallardo, and M. Martínez-Sánchez. Model of the plasma discharge in a Hall thruster with heat conduction. *Physics of Plasmas*, 9(9):4061–4070, 2002.

[22]E. Ahedo, P. Martínez-Cerezo, and M. Martínez-Sánchez. Steady and linearly-unsteady analysis of a Hall thruster with an internal sonic point. In *Proc. 36th Joint Propulsion Conference, Huntsville, AL*, AIAA 2000-3655. American Institute of Aeronautics and Astronautics, 2000.

[23]S. Tsikata, N. Lemoine, V. Pisarev, and D.M. Gresillon. Dispersion relations of electron density fluctuations in a hall thruster plasma, observed by collective light scattering. *Physics of Plasmas*, 16:033506, 2009.

[24]J.C. Adam, J.P. Boeuf, N. Dubuit, M. Dudeck, L. Garrigues, D. Gresillon, A. Heron, G.J.M. Hagelaar, V. Kulaev, N. Lemoine, et al. Physics, simulation and diagnostics of Hall effect thrusters. *Plasma Physics and Controlled Fusion*, 50:124041, 2008.

[25]S. Janhunen, A. Smolyakov, O. Chapurin, D. Sydorenko, I. Kaganovich, and Y. Raitses. Nonlinear structures and anomalous transport in partially magnetized exb plasmas. *Physics of Plasmas*, 25:11608, 2018.

[26]E. Ahedo and D. Escobar. Influence of design and operation parameters on Hall thruster performances. *Journal of Applied Physics*, 96(2):983–992, 2004.

[27]A.A. Litvak, Y. Raitses, and N.J. Fisch. Experimental studies of high-frequency azimuthal waves in Hall thrusters. *Physics of Plasmas*, 11:1701, 2004.

[28]Y.B. Esipchuk, A.I. Morozov, G.N. Tilinin, and A.V. Trofimov. Plasma oscillations in closed-drift accelerators with an extended acceleration zone. *Soviet Physics-Technical Physics*, 18:928–932, 1974.

[29]J.P. Boeuf. Tutorial: Physics and modeling of hall thrusters. *J. Applied Physics*, 121(1):011101, 2017.

[30]A.I. Morozov, Y.V. Esipchuk, A.M. Kapulkin, V.A. Nevrovskii, and V.A. Smirnov. Effect of the magnetic field on a closed-electron-drift accelerator. *Sov. Phys.-Tech. Phys.(Engl. Transl.) 17: No. 3, 482-7 (Sep 1972).*, 1972.

[31]W. Frias, A.I. Smolyakov, I.D. Kaganovich, and Y. Raitses. Long wavelength gradient drift instability in hall plasma devices. i. fluid theory. *Physics of Plasmas*, 19:072112, 2012.